Bimetallic Catalyst Particle Nanostructure. Evolution from Molecular Cluster Precursors

Michael S. Nashner, David M. Somerville, Philip D. Lane, David L. Adler,† John R. Shapley,* and Ralph G. Nuzzo*

Contribution from the School of Chemical Sciences and the Frederick Seitz Materials Research Laboratory, University of Illinois, Urbana, Illinois

Received June 27, 1996[⊗]

Abstract: A set of supported bimetallic catalysts, designated [Re_7Ir−N], [Re_7Ir−P], [Re_5IrRe_2−N], and [Re_5IrRe_2−P], has been prepared from two structural isomers (**1** and **2**) of the cluster compound $[Z]_2[Re_7IrC(CO)_{23}]$ (Z^+ = NEt_4^+, $N(PPh_3)_2^+$) by deposition onto high surface area alumina (≤1% Re) and activation in H_2 at 773 K. The specific activities of the catalysts for ethane hydrogenolysis at 500 K vary significantly (3−63 mmol of CH_4/mol of Re_7Ir per s) and depend on both the metal framework structure and the counterion present in the precursor. Interpretation of EXAFS data (from both Re and Ir L_3-edges) has enabled the development of specific models for the catalyst particle nanostructures that correlate with the catalytic activities. The more active catalysts ([Re_7Ir−N] and [Re_5IrRe_2−N]) are modeled by a hemisphere of close-packed (hcp) metal atoms (average diameter 1 nm) with Ir at the core. On the other hand, the less active catalysts ([Re_7Ir−P] and [Re_5IrRe_2−P]) are better described as two-dimensional layer structures. A combination of techniques, TPDE, IR, XANES, and EXAFS, applied under temperature-programmed conditions, has demonstrated that evolution of the final catalyst particle nanostructure depends on significant initial fragmentation of the cluster framework followed by preferential nucleation at iridium centers.

Introduction

There is intense interest in the structural and electronic properties of supported bimetallic clusters for technological as well as scientific reasons.[1−5] The modifications in the structural and electronic properties of active catalytic sites that result from the use of binary metal systems have allowed for dramatic improvements in the activity, selectivity, and robustness of catalysts for a variety of important processes, including naphtha reforming,[1,2] emissions control,[3] and electrocatalysis.[4] However, further progress in this area depends on developing an improved understanding of the fundamental rate/structure relationships for such catalytic materials.

One potentially promising approach to the controlled synthesis of supported nanoparticles involves the use of molecular carbonyl clusters as precursors.[5−12] Molecular metal clusters provide an ensemble of metal atoms with known composition and structure, and active metal particles are formed after dispersing the molecules and removing the CO ligands. In principle, the carbonyl cluster precursors provide a method for forming a narrow size distribution of active nanoparticles.[7] Furthermore, the use of heterometallic cluster precursors should afford improved control over the specific bimetallic composition of the catalytic species.[5,10−12] Specific evidence has been presented (based on catalytic selectivities and EXAFS) that the heterometallic cluster precursors can generate active catalytic sites that are not accessible from mixtures of homometallic precursors.[12] However, the issue of how the structures evolve on the surface of the support, from the molecular cluster precursor to catalytically active nanoparticle, remains of fundamental importance to the utility of this approach.

In the research described herein, we explore the structure and reactivity of supported metal catalysts resulting from the activation of the bimetallic cluster compound $[Re_7IrC(CO)_{23}]^{2-}$, which exists as two framework isomers: 1,4-$[Re_6C(CO)_{18}\{\mu_3\text{-}Re(CO)_3\}\{\mu_3\text{-}Ir(CO)_2\}]^{2-}$ and 1,3-$[Re_5IrC(CO)_{17}\{\mu_3\text{-}Re(CO)_3\}_2]^{2-}$ as shown in Chart 1.[13] Isomer **1** adopts a 1,4-bicapped octahedral structure, with one μ_3-$Re(CO)_3$ and one μ_3-$Ir(CO)_2$

Chart 1

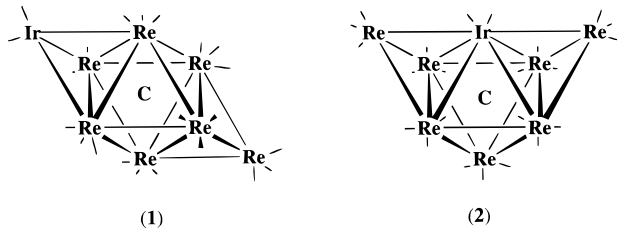

(**1**) 1,4-$[Re_6C(CO)_{18}\{\mu_3\text{-}Re(CO)_3\}\{\mu_3\text{-}Ir(CO)_2\}]^{2-}$

(**2**) 1,3-$[Re_5IrC(CO)_{17}\{\mu_3\text{-}Re(CO)_3\}_2]^{2-}$

† Current Address: KLA Instruments Corporation, San Jose, CA 95161.

⊗ Abstract published in *Advance ACS Abstracts,* December 15, 1996.

(1) Sinfelt, J. H. *Bimetallic Catalysts—Discoveries, Concepts, and Applications*; John Wiley & Sons: New York, 1983.

(2) Anderson, J. R. *Structure of Metallic Catalysts*; Academic Press: New York, 1975.

(3) Nunan, J. G.; Silver, R. G.; Bradley, S. A. In *Catalytic Control of Air Pollution*; Nunan, J. G.; Silver, R. G.; Bradley, S. A., Eds.; American Chemical Society: Washington, DC, 1992; pp 83−97.

(4) (a) Mukerjee, S.; Srinivasan, S.; Soriaga, M. P.; McBreen, J. *J. Electrochem. Soc.* **1995**, *142*, 1409. (b) McBreen, J.; Mukerjee, S. *J. Electrochem. Soc.* **1995**, *142*, 3399. (c) Radmilovic, V.; Gasteiger, H. A.; Ross, P. N., Jr. *J. Catal.* **1995**, *154*, 98.

(5) Ichikawa, M. *Adv. Catal.* **1992**, *38*, 283.

(6) Gates, B. C.; Guczi, L.; Knözinger, H. *Metal Clusters in Catalysis*; Elsevier: Amsterdam, 1986.

(7) Gates, B. C. *Chem. Rev.* **1995**, *95*, 511 and references therein.

(8) Klabunde, K. J.; Li, Y.-X. In *Selectivity in Catalysis*; American Chemical Society: Washington, DC, 1993.

(9) Iwasawa, Y. *Tailored Metal Catalysts*; Riedel: Boston, 1986.

(10) Fung, A. S.; McDevitt, M. R.; Tooley, P. A.; Kelley, M. J.; Koningsberger, D. C.; Gates, B. C. *J. Catal.* **1993**, *140*, 190.

(11) (a) Basset, J.-M.; Candy, J. P.; Chopin, A.; Nedez, C.; Quignard, F.; Santini, C. C.; Theolier, A. *Mater. Chem. Phys.* **1991**, *29*, 5. (b) Chopin, A.; Huang, L.; Theolier, A.; Gallezot, P.; Basset, J. M.; Siriwardane, U.; Shore, S. G.; Mathieu, R. *J. Am. Chem. Soc.* **1986**, *108*, 4224.

(12) Shapley, J. R.; Uchiyama, W. S.; Scott, R. A. *J. Phys. Chem.* **1990**, *94*, 1190.

(13) (a) Ma, L; Wilson, S. R.; Shapley, J. R. *J. Am. Chem. Soc.* **1994**, *116*, 787. (b) Ma, L. Ph.D. Thesis, University of Illinois at Urbana−Champaign, 1991.

S0002-7863(96)02174-9 CCC: $12.00

cap in *trans* positions. Isomer **2** is a 1,3-bicapped octahedron, where the Ir is incorporated into the octahedral carbide framework and connected to the two μ_3-Re(CO)$_3$ caps. Catalysts have been prepared by impregnation of high surface area alumina with solutions of the metal cluster salts followed by reduction in H_2 at 773 K. We refer to the activated catalysts prepared in this way as [Re_7Ir-N] and [Re_5IrRe_2-N] or [Re_7Ir-P] and [Re_5IrRe_2-P] for materials derived from the corresponding metal framework isomers crystallized as the $[NEt_4]^+$ (TEA) and $[N(PPh_3)_2]^+$ (PPN) salts, respectively. The reactivity was monitored by using ethane hydrogenolysis as a structure-sensitive catalytic process.[14] To our knowledge, the Re−Ir bimetallic catalyst system has not been studied previously, although there has been considerable attention focused on the Pt−Re and Pt−Ir systems, since these combinations are employed as industrial reforming catalysts.[1,15,16]

Structural studies of the supported catalysts described here have been performed by using *in situ* extended X-ray absorption fine structure (EXAFS) and X-ray absorption near-edge (XANES) spectroscopies. An issue of general interest considered in this work is the unique insights provided by the relatively high Re:Ir ratio for these cluster precursors. This composition allows us to clearly demonstrate the structures of the catalytic nanoparticles, which show a strong tendency for the segregation of the Ir atoms to metal rich (i.e., high coordination number) environments of the particle.

Experimental Section

Preparation of Supported Re−Ir Catalysts. In order to improve handling of the flocculent alumina (Degussa, Aluminumoxid C), it was wetted with deionized water and then dried at 115 °C for ca. 12 h. The resulting chunks were crushed and sieved (180−250 μm). A typical surface area of 90−100 m^2/g was found by nitrogen adsorption BET measurements.[17] The cluster precursors, prepared using literature procedures,[13a] were dissolved in acetone, and ca. 500 mg samples of alumina were impregnated with the solution to incipient wetness (0.5 wt % metal loading). These samples were allowed to dry briefly in air prior to being loaded in the reactor.

Catalytic Studies. The supported samples were activated and tested on a catalyst line that included a gas handling system, catalytic reactor, and equipment for analysis of the effluent.[17,18] Streams of H_2 (Matheson, 99.95%) and C_2H_6 (Matheson, 99.0%) were deoxygenated over Cr^{II}/SiO_2 and dried over activated molecular sieves. The Pyrex U-tube reactor contained a course frit supporting the catalyst bed, which was in contact with a thermocouple well containing an Omega type-k chromel/alumel thermocouple. The reactor was heated by a tube furnace controlled with an Omega CN2011 temperature controller. A Packard model 430 gas chromatograph with a flame ionization detector was used to separate and quantify the hydrocarbon products ($^1/_8$ in. × 7 ft, 10 wt % *n*-octane/Porasil column). The effluent was also monitored by a computer-interfaced Dyco quadrupole mass spectrometer (model M100M), which was connected immediately downstream from the reactor by a silica capillary.

Prior to activation, each sample was evacuated for 1 h to remove residual solvent adsorbed on the alumina. The samples were activated by heating to 773 K (at 15 K/min) under a stream of H_2 (40 mL/min) and holding at 773 K for 1 h. The samples were cooled to the appropriate temperature under a continuous stream of H_2, then C_2H_6 was introduced into the gas flow (H_2:C_2H_6 = 40:4 mL/min). Constant conversion of C_2H_6 to CH_4 typically was achieved in ca. 5−10 min. Catalytic studies were carried out at temperatures for which the conversion of C_2H_6 was held below 10% (450−575 K). To change the temperature, the C_2H_6 flow was turned off, and then the sample was warmed by 25−50 K under H_2 only until the CH_4 detected reached baseline levels. The sample was then heated or cooled to the next desired temperature, and the process was repeated. Potential deactivation of the catalyst was monitored by periodically checking the percent conversion at a previously used temperature; changes of less than 10% were deemed satisfactory.

Infrared Spectroscopy. Supported samples for infrared studies were prepared by incipient wetness as described above (0.5 wt % metal loading). The samples were allowed to dry briefly in air, then pressed into wafers (150 mg × 2 cm diameter) suitable for infrared transmittance studies. The wafers were loaded into a temperature-controlled (T_{max} = 573 K) infrared cell (Harrick Scientific model HTC-100), having KBr windows sealed with Viton O-rings, which was then purged with H_2. Samples were heated in flowing H_2 (40 mL/min) and infrared spectra were recorded at the desired temperature with a Perkin-Elmer 1750 FT-IR spectrometer. Background spectra were determined from an alumina wafer treated in an analogous fashion.

Temperature-Programmed Decomposition (TPDE) in Hydrogen. Supported samples (500 mg, 0.5 wt % metal) were prepared as described above and loaded into the U-tube reactor. The samples were heated at 15 K/min under flowing H_2 (40 mL/min) from 298 to 773 K while monitoring by mass spectrometry at m/z = 16 (CH_4), 28 (CO, C_2H_6), and 78 (C_6H_6). Since both CO and C_2H_6 produce major peaks at m/z = 28, the detection of C_2H_6 separately from CO was established by observation of the C_2H_6 signal at m/z = 27; under some circumstances gas chromatography also was used.

X-ray Absorption Spectroscopy (XAS). All XAS measurements were performed in a Lytle-style catalyst cell (the EXAFS Company). The cell allowed *in situ* X-ray fluorescence measurements with an operating temperature up to 773 K. A metered flow of H_2 (Matheson, 99.999%) was passed through traps (Chromatography Research Supplies) to remove O_2 and water before entering the cell. To avoid oxygen contamination during the experiments, the interior reactor volume immediately surrounding the sample was continuously purged with H_2, and the shielding volume surrounding the reactor was purged with He (Matheson, 99.995%). Immediately after adsorbing the cluster precursor on alumina, the supported sample (ca. 200 mg) was pressed into a pellet (1 mm × 10 mm). The pellet was fastened to the sample mount of the cell, which was then purged with H_2 for 1 h. The temperature was monitored with an Omega type-k chromel/alumel thermocouple mounted directly on the sample stage. The supported samples were activated by heating them at 15 K/min in flowing H_2 (40 mL/min) to a temperature of 773 K and holding at that temperature for 1 h. In some runs, the Re L_3 near edge region (XANES) was repeatedly scanned during the activation process. The samples were then cooled to room temperature before making the EXAFS measurements.

EXAFS data were taken on both the Re and Ir L_3-edges. The energy range was limited to about 650 eV because of the overlap of the Re and Ir L-edges. Fluorescence data from the reference compounds ReO_3 and $ReSi_2$ (Aldrich) were also measured in the cell. The ReO_3 and $ReSi_2$ powders were finely ground and uniformly dispersed on filter paper to a thickness of less than 10 μm as determined optically with a microscope. Data were obtained for Re metal powder (Aldrich) in both transmission and fluorescence modes; the latter required a 10% correction to the EXAFS amplitude to compensate for self-absorption.[19]

X-ray absorption data were measured at the National Synchrotron Light Source, located at Brookhaven National Laboratory, Upton, New York. Data for Re were taken on the North Carolina State University beamline X11B. All other data were obtained on the UIUC/AT&T X16C beamline which uses a sagitally-focusing Si(111) crystal monochromator to focus 3.5 mrad of light into a 0.3 mm × 2 mm beam spot at the sample. The focusing dynamically follows the energy to maintain the beam spot profile over the scan. The initial beam intensity (I_0) was measured with a 6-in. ion chamber containing a 1:1 mixture of He and N_2. The fluorescence was measured with a Lytle detector

(14) (a) Sinfelt, J. H. *Adv. Catal.* **1973**, *23*, 91. (b) Sinfelt, J. H. *Acc. Chem. Res.* **1977**, *10*, 15. (c) Sinfelt, J. H. *Catal. Lett.* **1991**, *9*, 159.

(15) Biswas, J.; Bickle, G. M.; Gray, P. G.; Do, D. D.; Barbier, J. *Catal. Rev. Sci. Eng.* **1988**, *30*, 161.

(16) Xiao, J.; Puddephatt, R. J. *Coord. Chem. Rev.* **1995**, *143*, 457.

(17) Lane, P. D. Ph.D. Thesis, University of Illinois at Urbana−Champaign, 1995.

(18) Urbancic, M. A. Ph.D. Thesis, University of Illinois at Urbana−Champaign, 1984.

(19) Tan, Z.; Budnick, J. I.; Heald, S. M. *Rev. Sci. Instrum.* **1989**, *60*, 1021.

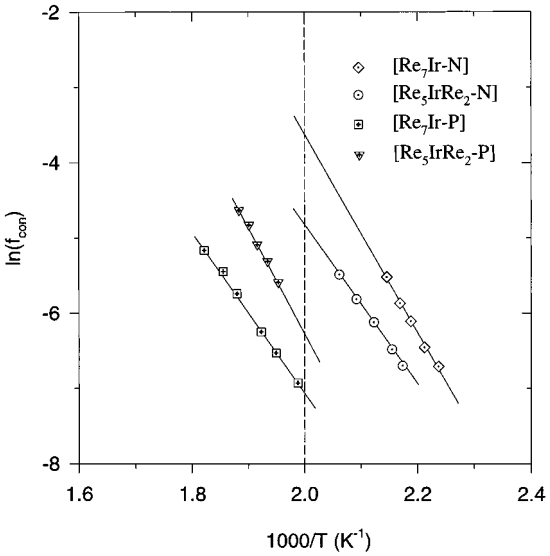

Figure 1. Arrhenius plots for C_2H_6 hydrogenolysis: (diamond) [Re_7-Ir−N)]; (circle) [Re_5IrRe_2−N]; (square) [Re_7Ir−P]; (triangle) [Re_5-$IrRe_2$−P].

filled with Ar and placed at 90° to the incident beam. Before taking data on each sample, the energy of the beam was calibrated to the inflection point of the Re L_3-edge threshold by using a sample of Re metal.

The EXAFS data analysis was performed by following the technique of Kincaid et al.[20,21] The background was subtracted in *k*-space by using a least-squares fit to a cubic spline function with two knots. The Fourier-filtered, k^2-weighted data were fit in *k*-space by nonlinear least-squares refinement to either a two- or a three-shell model, as appropriate, to determine nearest neighbor distances, relative threshold energy (ΔE_0), the coordination number, and the relative Debye−Waller factor ($\Delta\sigma^2$) for each shell. A Hanning window function was used to select the shells for analysis. Since scattering from Re and Ir neighbors could not be distinguished in this analysis,[20] both were modeled using the Re−Re scattering function taken from Re metal. A Re−O absorber−scatterer pair from ReO_3 was used to model the M−O, M−N, and M−C scattering neighbors, and Re−Si from $ReSi_2$ was used to model M−Al or M−P scattering (where M = Re or Ir). For the Re XANES data, the step height was normalized by straight line fits to the pre-edge and post-edge (>100 eV) regions.

Results

1. Characterization of Catalytically Active Nanoparticles. (a) Hydrogenolysis of Ethane. Arrhenius plots were constructed from the normalized fractional conversion of C_2H_6 measured at several temperatures during the steady-state hydrogenolysis of ethane (Figure 1). The calculated activation energies (21−28 kcal/mol) were similar to those reported for conventionally prepared Re/alumina catalysts (27 kcal/mol),[17] and lower than that reported for conventional Ir/alumina (43.5 kcal/mol).[22] In order to compare the relative activities of the four cluster-derived catalysts, the straight line fit to the data in the Arrhenius plot was extended to 500 K, and a normalized turnover frequency (TOF) at this common temperature was then calculated for each catalyst (see Table 1).

(b) Extended X-ray Absorption Fine Structure. Figure 2 compares the Fourier-transformed Re metal EXAFS data (for a *k*-range of ca. 3 to 12.5 $Å^{-1}$) with the averaged EXAFS

Table 1. Hydrogenolysis of Ethane

catalyst	E_a (kcal/mol)	temp range (K)	TOF at 500 K[a] (mmol of CH_4/mol of [Re_7Ir] per s)
[Re_7Ir−N]	27(2)	450−470	63(20)
[Re_5IrRe_2−N]	21.7(0.5)	460−490	21(1)
[Re_5IrRe_2−P]	28(2)	540−575	5.2(0.8)
[Re_7Ir−P]	21.6(0.5)	500−550	3.0(0.1)

[a] Error was estimated by the extrapolation of the 90% confidence limits (1.65σ) of the linear regression fit.

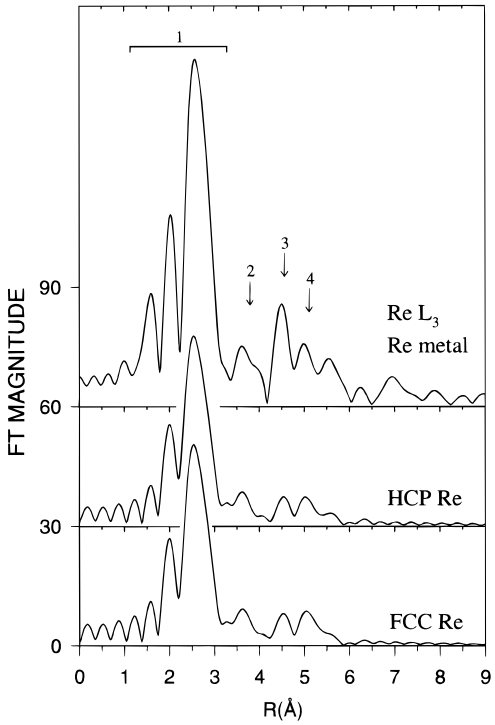

Figure 2. Fourier transformed k^2-weighted EXAFS data from the Re L_3-edge of Re metal (k = ca. 3 to 12.5 $Å^{-1}$), and average EXAFS calculated with FEFF for 26-atom hcp and 28-atom fcc hemispherical nanoclusters, respectively. Arrows denote the peaks that correspond to the R_1−R_4 shells as described in the text.

calculated using FEFF for two model structures for "close-packed" nanoclusters. The bulk shell structure of hexagonal close-packed (hcp) Re metal consists of 12 nearest neighbors at 2.75 Å, 6 neighbors at 3.89 Å, 2 neighbors at 4.46 Å, 18 neighbors at 4.78 Å, 12 neighbors at 5.24 Å, and 6 neighbors at 5.52 Å. The Re metal radial structure function shown in the figure (not phase corrected) contains easily discernible contributions from the 12 nearest neighbors at 2.75 Å (R_1), 6 neighbors at 3.89 Å (R_2), 18 neighbors at 4.78 Å (R_3), and 12 neighbors at 5.24 Å (R_4). The splitting seen in the first-shell peak (ca. 2.3 Å) is the result of a Ramsauer−Townsend resonance.[20] In addition, the low atomic number (Z) bonding contributions seen at distances shorter than the first metal shell (R_1) (ca. 1.6 Å) are believed to be due to surface oxidation.

In the present work, we are concerned with the catalytic properties and structural habits evidenced by nanoscale metal particles. The EXAFS data which define the latter show strong influences which result directly from the limited size of the particle and relatively large numbers of atoms which reside at low coordination number sites (e.g., at the surface or support interface, etc.). Thus to provide a point for comparison, the radial structure functions were calculated for two model hemispherical nanoparticles using FEFF (Figure 2). Each particle was constrained to a diameter of ca. 11 Å and constructed with either a hcp or a face-centered cubic (fcc) structure. The reduced EXAFS amplitude (i.e., lower coordina-

(20) Lee, P. A.; Citrin, P. H.; Eisenberger, P.; Kincaid, B. M. *Rev. Mod. Phys.* **1981**, *53*, 769.
(21) Teo, B. K. *EXAFS: Basic Principles and Data Analysis*; Springer-Verlag: New York, 1986.
(22) Foger, K.; Anderson, J. R. *J. Catal.* **1979**, *59*, 325.
(23) Rupp, B.; Smith, B.; Wong, J. *Comput. Phys. Commun.* **1992**, *67*, 543.

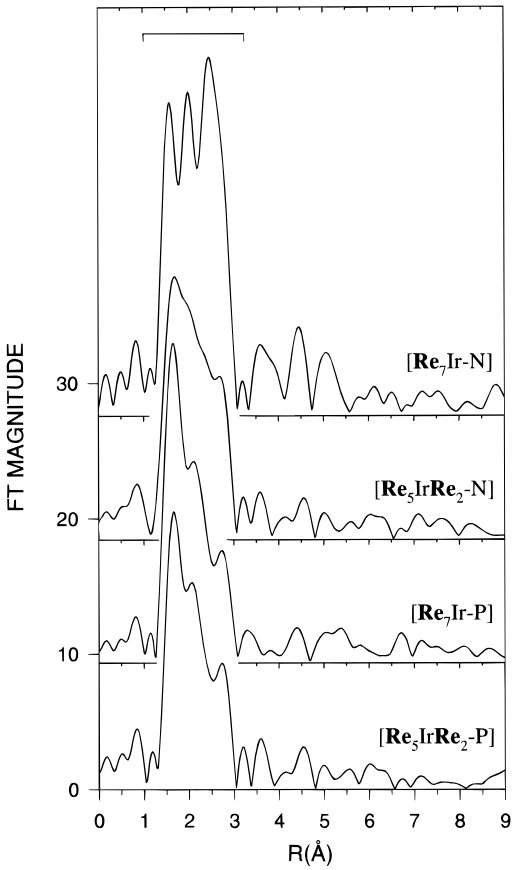

Figure 3. Comparison of the Fourier transformed, k^2-weighted EXAFS data for the Re L_3-edge of the activated catalysts collected at 300 K (k = ca. 3 to 12.5 Å^{-1}). The bracket shown in each figure indicates the Hanning filter width used to select the first shells in the analysis.

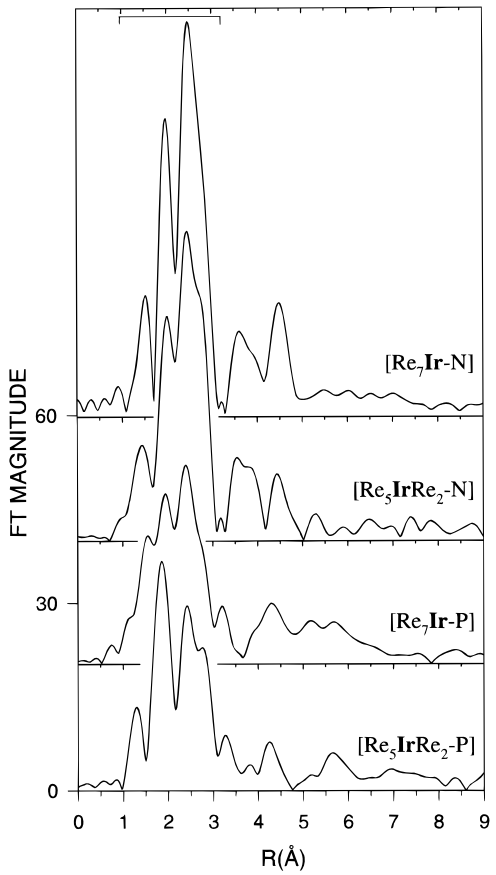

Figure 4. Comparison of the Fourier transformed, k^2-weighted EXAFS data for the Ir L_3-edge of the activated catalysts at 300 K (k = ca. 3 to 12.5 Å^{-1}). The bracket shown in each figure indicates the Hanning filter width used to select the first shells in the analysis.

tion numbers) seen for shells R_1-R_4 in the model nanoclusters demonstrates the large perturbation which results from scattering weighted by a significant fraction of surface atoms. The subtle differences which exist between the fcc and hcp crystal structures are not resolved in the EXAFS data of the model nanoparticles, however. The most significant point to note from these results is that the first and more distant metal shell amplitudes are expected to show sensitivities to cluster size and that these effects are less diagnostic of an underlying hcp or fcc habit in a "close-packed" motif. To simplify the analyses and interpretations which follow, we therefore use inferences derived from analysis based on a hcp model. We defer further discussion on this point to later.

Figures 3 and 4 display the Fourier transforms of the k^2-weighted EXAFS data for the Re and Ir L_3-edges, respectively, for all the catalysts. Quantitative structural parameters from the first shell EXAFS data of the catalyst material were extracted by fitting the Fourier-filtered Re and Ir EXAFS data with phase shift and amplitude functions determined from bulk Re metal and ReO_3 model compounds. The brackets indicate the limits of the Hanning window function used to isolate and Fourier filter the first shell data. Because of the overlap of the first metal shell and the low-Z shell(s), they were analyzed together using a two- or three-shell model as appropriate (see below). The low-Z contributions found around the Re and Ir centers were fit with the Re−O scattering function of the ReO_3 model; because of the similarities in their EXAFS scattering functions, the presence of N and C cannot be excluded, however.

As discussed in detail below, a best fit to the Ir EXAFS in the [Re_7Ir−N] catalyst was obtained with a two shell fit with 10.8 Ir−M (Re−Re model) scatterers at 2.71 Å and about one (1.3) Ir−O (Re−O model) scatterer at 2.52 Å. The best fit to the corresponding Re L_3 edge data requires 5.1 Re−M and about one (0.7) Re−O scatterers at similar distances as well as another scatterer (1.1) at 2.05 Å. Because the uncertainty in the coordination numbers for the low-Z bonds is relatively large, due to their small contribution to the total EXAFS amplitude, we will focus our analysis on the metal coordination contributions. The fitting results for the Re and Ir first shell data are presented in Tables 2 and 3, respectively.

As confirmed by quantitative fitting of the first shell EXAFS data, as described before, the predominant difference between the catalysts is the nature of the metal coordination environment present in each. The low-Z contributions evident around Re were best fit by models involving contributions from low-Z neighbors at 2.1 and 2.5 Å, whereas the Ir required only a single low-Z scatterer at 2.5 Å. We found no significant improvement by adding a Re−P shell for the PPN counterions. The fitting results for the first-shell data obtained for the four compounds are presented in Tables 2 and 3. It can be seen that significant first shell metal coordination characterizes the Ir centers in all fully activated catalysts; the first shell metal coordination numbers for Re are significantly lower, however.

In addition to the first metal shell coordination found in the Re and Ir EXAFS data from the [Re_7Ir−N] catalyst, significant higher-shell coordination (i.e., R_2-R_4) indicates the elements of a close-packed shell structure. Interestingly, the Ir data indicate large magnitude for the first three shells only, while the Re shows a lower magnitude, but surprisingly includes measurably significant intensity from the fourth shell (see Figures 3 and 4). The [Re_5IrRe_2−N] catalyst shows a similar shell structure around Ir albeit with a significant decrease in

Table 2. Re First-Shell Parameters Determined by Fitting the Re L_3-Edge EXAFS Data[a]

			first shell parameters			
catalyst	temp (K)	shell[b]	N	R (Å)	$\Delta\sigma^2$ (Å^2)[c]	ΔE_0 (eV)[d]
[Re_7Ir−N]	773	Re−M	5.1	2.71	0.002	−0.1
		Re−O	0.7	2.55	0.002	7.0
		Re−O	1.1	2.05	0.001	1.2
	673	Re−M	4.0	2.69	0.005	−2.3
		Re−O	0.7	2.53	0.002	7.5
		Re−O	1.0	2.07	0.001	−4.2
[Re_5IrRe_2−N]	773	Re−M	4.2	2.70	0.003	−2.4
		Re−O	0.6	2.53	0.002	9.0
		Re−O	1.4	2.05	0.002	0.8
	673	Re−M	1.9	2.67	0.005	−0.6
		Re−O	0.8	2.56	0.003	5.4
		Re−O	1.1	2.09	0.002	−3.8
[Re_7Ir−P]	773	Re−M	1.8	2.71	0.003	−5.0
		Re−O	0.6	2.56	0.002	5.2
		Re−O	0.7	2.08	0.001	−2.6
[Re_5IrRe_2−P]	773	Re−M	2.4	2.69	0.004	−1.8
		Re−O	0.6	2.56	0.001	6.4
		Re−O	1.2	2.06	0.001	−0.4

[a] Estimated precision: N, ±20%; R, ±0.02 Å. All $k^2\chi(k)$ EXAFS data, fits, and fit residuals are available in the Supporting Information. [b] The Re−M absorber−backscatterer pair was modeled with first-shell Re metal EXAFS data (12 neighbors at 2.75 Å). The Re−O absorber−backscatterer pair was modeled with a Re−O absorber−scatterer pair from the first Re−O shell (6 O neighbors at 1.89 Å) measured from ReO_3. [c] The difference in the Debye−Waller factor (σ^2) with respect to the reference compound. [d] The change in threshold energy (E_0) with respect to the reference (correction in the relative edge positions).

Table 3. Ir First-Shell Parameters Determined by Fitting the Ir L_3-Edge EXAFS Data[a]

			first shell parameters			
catalyst	treatment temp (K)	shell[b]	N	R (Å)	$\Delta\sigma^2$ (Å^2)[c]	ΔE_0 (eV)[d]
[Re_7Ir−N]	773	Ir−M	10.8	2.71	0.002	5.0
		Ir−O	1.3	2.52	0.008	3.8
	673	Ir−M	8.4	2.71	0.003	2.2
		Ir−O	0.9	2.54	0.006	1.2
	623	Ir−M	6.0	2.70	0.003	5.4
		Ir−O	0.9	2.56	0.002	1.8
	573	Ir−M	0			
[Re_5IrRe_2−N]	773	Ir−M	9.0	2.70	0.003	7.1
		Ir−O	1.2	2.55	0.007	4.7
	673	Ir−M	7.1	2.69	0.004	7.8
		Ir−O	1.0	2.49	0.008	5.2
	573	Ir−M	6.0	2.69	0.004	6.0
		Ir−O	2.1	2.13	0.008	1.2
[Re_7Ir−P]	773	Ir−M	4.8	2.71	0.002	3.0
		Ir−O	1.1	2.60	0.004	1.4
		Ir−O	1.8	2.07	0.006	−5.3
[Re_5IrRe_2−P]	773	Ir−M	5.5	2.70	0.002	3.0
		Ir−O	0.8	2.51	0.004	2.0
		Ir−O	1.2	2.16	0.002	−8.0

[a] Estimated precision: N, ±20%; R, ± 0.02 Å. All $k^2\chi(k)$ EXAFS data, fits, and fit residuals are available in the Supporting Information. [b] The Ir−M absorber−backscatterer pair was modeled with first-shell Re metal EXAFS data (12 neighbors at 2.75 Å). The Ir−O absorber−backscatterer pair was modeled with a Re−O absorber−scatterer pair from the first Re−O shell (6 O neighbors at 1.89 Å) measured from ReO_3. [c] The difference in the Debye−Waller factor (σ^2) with respect to the reference compound. [d] The change in threshold energy (E_0) with respect to the reference (correction in the relative edge positions).

magnitude. In contrast, the Re data for [Re_5IrRe_2−N] reveal very little structure above the noise level for the second through fourth shells. In the [Re_7Ir−P] and [Re_5IrRe_2−P] catalysts, the Ir higher shell structure is limited to wide peaks at roughly 4.8 and 5.5 Å, and there is no significant evidence of higher shell structure around the Re atoms. With regard to all the data shown in Figures 3 and 4, it is important to note that the noise level seen at distances corresponding to even the fourth metal coordination shell is exceptional (this is most easily illustrated by inspection of the noise seen at distances greater than 6 Å).

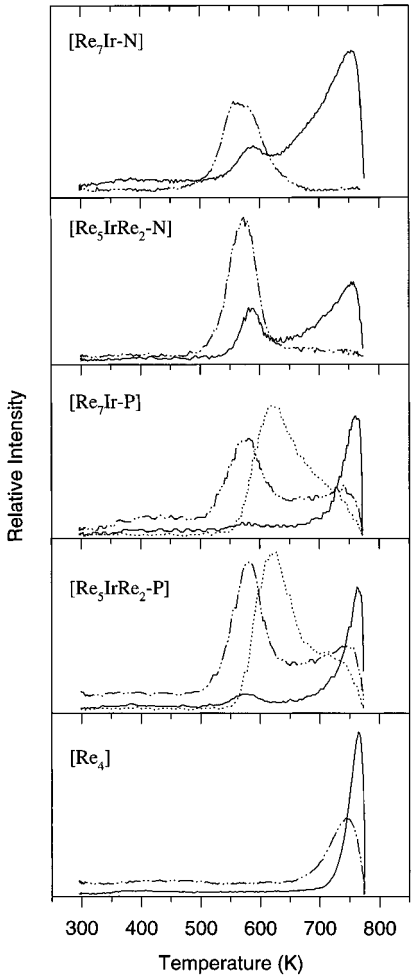

Figure 5. Temperature programmed decomposition (TPDE) in H_2 with m/z = 16 (—), 28 (—••—), and 78 (•••) of [Re_7Ir−N], [Re_5IrRe_2−N], [Re_7Ir−P], [Re_5IrRe_2−P], and [$Re(CO)_3OH]_4$ on Al_2O_3.[17]

The Re and Ir EXAFS data were also collected under typical hydrogenolysis conditions. In a prototypical experiment, both the Re and Ir data indicated no significant changes occurred in the metal shell structure of the catalyst after flowing a H_2:C_2H_6 mixture (40:20 mL/min) at 473 K for 30 min. In addition, the metal structure of a representative catalyst was examined for sensitivity to cycles of oxidation and re-reduction. After flowing O_2 (40 mL/min) at room temperature both the Re and Ir EXAFS indicated the formation of metal−oxygen bonds at the expense of metal coordination. After re-reduction in H_2 at 773 K the initial metal shell structure around both Re and Ir was reformed.

2. Cluster Fragmentation and Nanoparticle Nucleation. (a) Temperature-Programmed Decomposition (TPDE) in Hydrogen. Activating the alumina-supported cluster precursors in H_2 resulted in the desorption of CO and CH_4 from all samples. In addition, C_2H_6 or C_6H_6 desorption was observed when the precursors involved either the TEA or PPN counterion, respectively. The data showing the evolution of these products during activation are presented in Figure 5 for each sample. The analogous profiles for a Re-only precursor, $\{Re(CO)_3(\mu_3\text{-}OH)\}_4$, are included for comparison.

The TPDE profiles were strongly dependent upon the choice of counterion. Samples containing TEA desorbed CO with a single maximum near 575 K, whereas samples containing PPN desorbed CO with two maxima, one near 575 K and a second near 750 K. Methane was evolved from the PPN-based samples

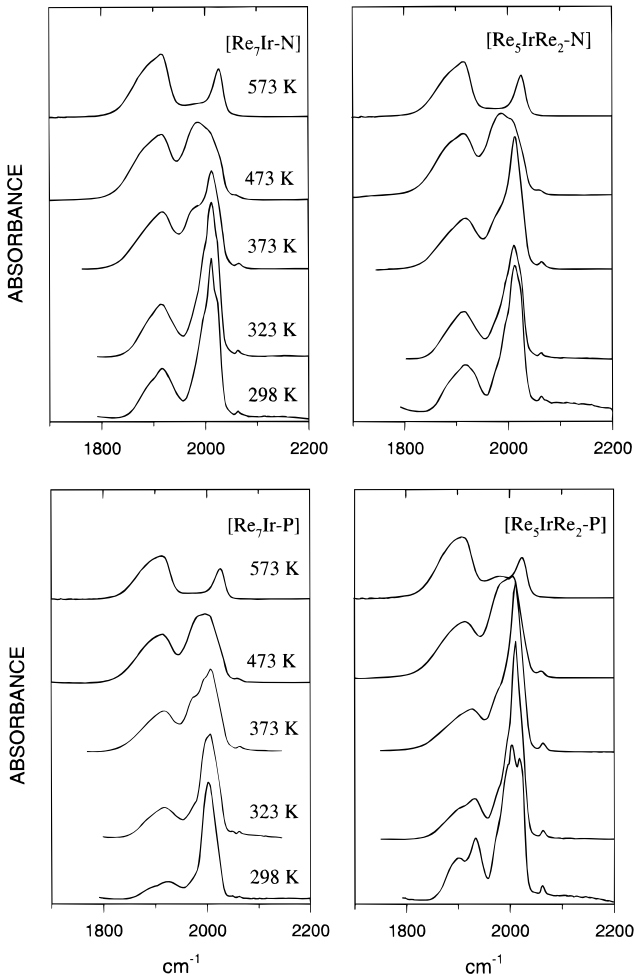

Figure 6. Infrared spectra collected at the indicated temperatures: (a) [Re_7Ir-N]; (b) [Re_5IrRe_2-N]; (c) [Re_7Ir-P]; (d) [Re_5IrRe_2-P].

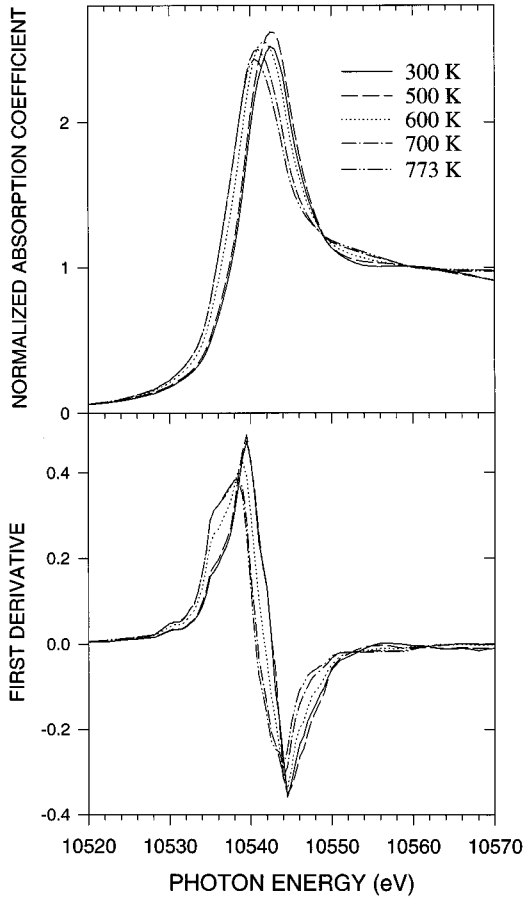

Figure 7. Comparison of the Re L_3 near edge region of [Re_7Ir-N] during activation in H_2. Upper: normalized absorption spectra. Lower: first derivative spectra.

only above 650 K with a maximum centered near 760 K; the TEA-based samples also evolved CH_4 at 760 K but desorbed additional CH_4 at lower temperatures (near 600 K). However, this latter quantity of CH_4 likely results from hydrogenolysis of TEA, since C_2H_6 desorption from TEA decomposition occurred at the same temperature. Benzene desorption (from hydrogenolysis of the PPN counterion) began at 560 K with a maximum at 625 K followed by a higher temperature shoulder.

(b) Infrared Spectroscopy. Activation of the supported samples was monitored by IR spectroscopy to a temperature of 573 K (Figure 6). The spectra for the different precursors were qualitatively similar at each temperature. At 298 and 323 K, the supported clusters showed strong CO bands with maxima at 2014 and 1914 cm^{-1}. Shoulders were apparent at 2023 and 1985 cm^{-1}. Upon heating the samples in H_2, the intensity of the peak at 2014 cm^{-1} diminished while that for the peaks at 1914, 1985, and 2023 cm^{-1} increased. At 573 K, the peak at 2014 cm^{-1} had disappeared for all samples while the peaks at 1914 and 1985 cm^{-1} were still strong. At 573 K, the peaks at 1914 and 2023 cm^{-1} remained evident, whereas the peak at 1985 cm^{-1} was absent. The behavior of the peak at 2023 cm^{-1} as a function of temperature was difficult to determine due to overlap with other bands. Changes in the spectra of the supported [Re_5IrRe_2-P] sample appeared to occur more slowly, as demonstrated by the similarity of the 298 K spectrum to that of the acetone solution spectrum[13] as well as the presence of a residual 1985-cm^{-1} peak even at 573 K.

(c) X-ray Absorption Near-Edge Structure (XANES). Figure 7 displays the Re L_3 near-edge region taken during activation of the [Re_7Ir-N] sample. The sharp peak, or white line, at the Re L_3-edge is an absorption-threshold resonance which is attributed to electronic transitions from filled Re $2p_{3/2}$ states to vacant 5d states and is therefore sensitive to changes in electron occupancy in the valence orbitals of the absorber.[24] As a consequence, resonance intensity is affected by changes in oxidation state; however, more subtle effects such as the dispersion or changes in the interaction with the support are also important.[24d,e]

The resonance intensity increased to a maximum at ca. 500 K; no change was evident in the binding energy at this stage. When the sample was heated to 600 K, the intensity decreased and the edge shifted ca. 1 eV to lower binding energy. The resonance intensity fell to a minimum after heating for 1 h at 773 K and a minimum in the binding energy of 10537 eV was also noted. Similar changes in the near-edge structure were observed for the [Re_5IrRe_2-N], [Re_7Ir-P], and [Re_5IrRe_2-P] samples; the maximum white line intensity was reached at essentially the same temperature ($\pm$10 K) for each, and the final intensities were the same to within $<$5%.

The first derivative of the Re L_3 near-edge absorption spectra (shown in Figure 7 for [Re_7Ir-N]) exhibited subtle changes in the absorption-threshold resonance. In each first-derivative spectrum, the positive peak had a low-energy shoulder. Interestingly, changes in the relative intensity of the main peak and shoulder occurred coincident with the shifts to lower binding

(24) (a) Lytle, F. W. *J. Catal.* **1976**, *43*, 376. (b) Mansour, A. N.; Cook, J. W.; Sayers, D. E. *J. Phys. Chem.* **1984**, *88*, 2330. (c) Mansour, A. N.; Cook, J. W.; Sayers, D. E. *J. Phys. Chem.* **1984**, *88*, 2330. (d) Meitzner, G.; Via, G. H.; Lytle, F. W.; Sinfelt, J. H. *J. Phys. Chem.* **1992**, *96*, 4960. (e) Sinfelt, J. H.; Meitzner, G. D. *Acc. Chem. Res.* **1993**, *26*, 1.

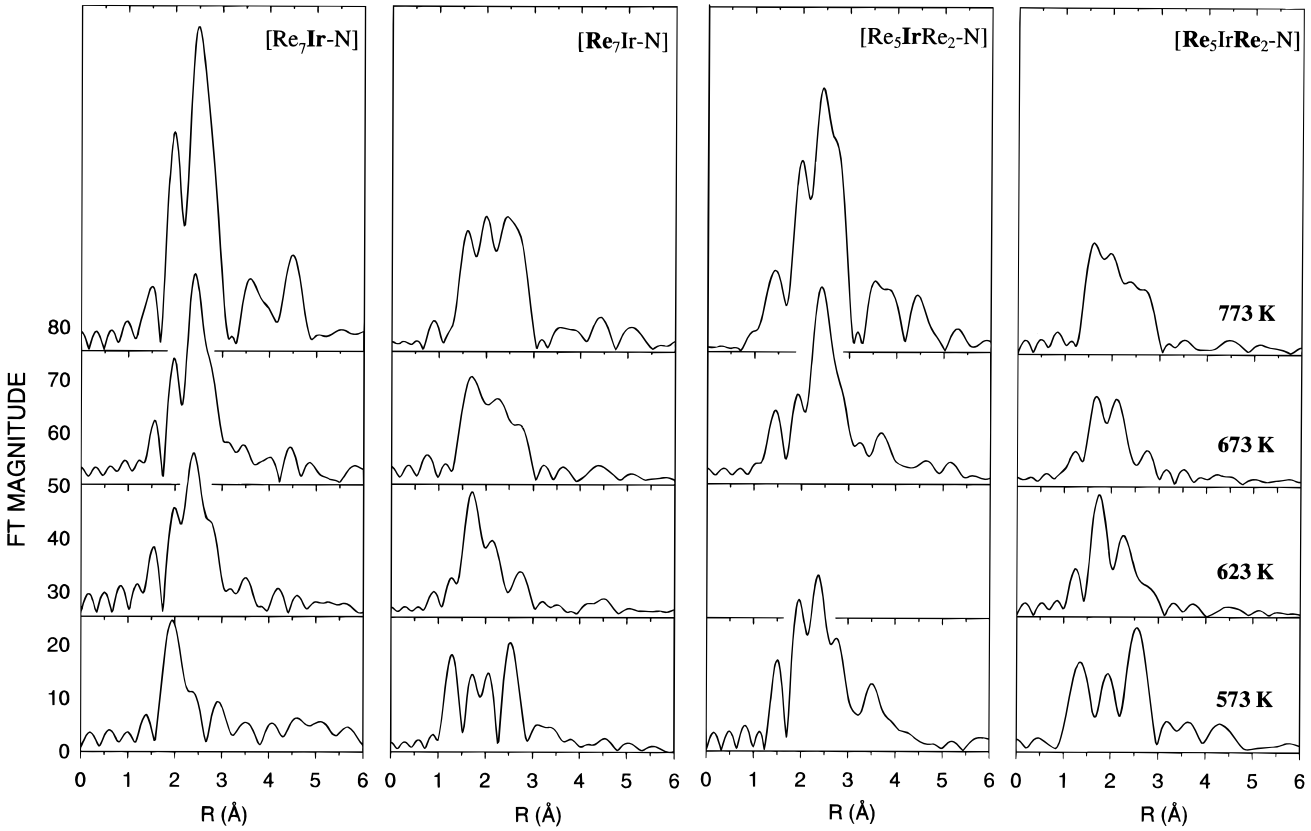

Figure 8. Comparison of the Fourier transformed, k^2-weighted EXAFS data for the Re and Ir L_3-edges of $[Re_7Ir-N]$ and $[Re_5IrRe_2-N]$ at the indicated temperature during activation in H_2.

energy which were found to occur during the activation process. The low energy shoulder (10536 eV), apparent at 300 and 500 K, increases markedly in magnitude while heating in H_2 from 600 to 773 K. After an hour at 773 K there was little additional change noted in the peak structure.

(d) Temperature-Dependent Extended X-ray Absorption Fine Structure. The EXAFS associated with the Re and Ir L_3 edges in the TEA-based samples after treatment at various temperatures is illustrated in Figure 8. The Fourier transform of the k^2-weighted data provides a convenient representation of the qualitative changes occurring in the ordered coordination environment of the Re and Ir atoms in the two samples. Changes in magnitude indicate an increase in the metal coordination and a decrease in low-Z coordination with higher annealing temperatures for both Re and Ir. Quantitative structural parameters were extracted by fitting the Re and Ir EXAFS data as described above (k^2-weighted data, fits, and residuals are available in the Supporting Information).

At low annealing temperatures (ca. 600 K), the Re EXAFS data reveal a large degree of static disorder, which suggests a diverse Re coordination environment. Qualitatively, the coordination environment of Re seen after heating the samples to 573 K consists of low-Z neighbors at several coordination distances with negligible near-shell metal coordination. The peak in the Fourier-transform trace at 2.6 Å is likely due to a Re−C−O multiple scattering interaction from remaining carbonyl species. Heating either sample to 623 K resulted in the loss of this feature. Heating further to 673 K increased the order of the Re environment; at this point three shells are required to fit the EXAFS data, a metal shell at 2.7 Å and two Re−O shells. The results of the fits are shown in Table 2. The major difference seen between the isomers was the relative metal-coordination numbers for the Re atoms at each temperature. These differences are summarized in Table 4.

Table 4. Comparison of the Re and Ir First-Shell Metal Coordination Numbers Determined by Fitting the EXAFS Data[a]

		first-shell coordination[b]	
catalyst	treatment temp (K)	Re−M[c]	Ir−M
$[Re_7Ir-N]$	773	5.1	10.8
	673	4.0	8.4
	623		6.0
	573		0
$[Re_5IrRe_2-N]$	773	4.2	9.0
	673	1.9	7.1
	573		6.0
$[Re_7Ir-P]$	773	1.8	4.8
$[Re_5IrRe_2-P]$	773	2.4	5.5

[a] Coordination numbers were taken from Tables 2 and 3. [b] Only M−M bond distances that fell between 2.69 and 2.72 Å were included. [c] At treatment temperatures ≤623 K no Re−M (at ca. 2.7 Å) contributions could be fit to the Re EXAFS data.

The Fourier-transformed Ir EXAFS data showed similar trends. Interestingly, when the $[Re_5IrRe_2-N]$ sample was heated to 573 K in H_2 it showed the presence of a metal shell at about 3.5 Å which may be due to the presence of remaining clusters or cluster fragments on the support. In contrast, the $[Re_7Ir-N]$ Ir EXAFS data taken after annealing in H_2 at 573 indicated only low-Z coordination. Quantitative fitting results indicated that the Ir shell structure obtained by heating either of these latter two samples to >673 K consisted predominantly of metal scatterers with only a small low-Z contribution. The results of these fits are presented in Table 3 and the relative trends summarized in Table 4.

Discussion

1. Structural Characterization of Catalytically Active Re−Ir Nanoparticles. The dramatic differences seen in the Re−M and Ir−M coordination numbers given in Table 4 show

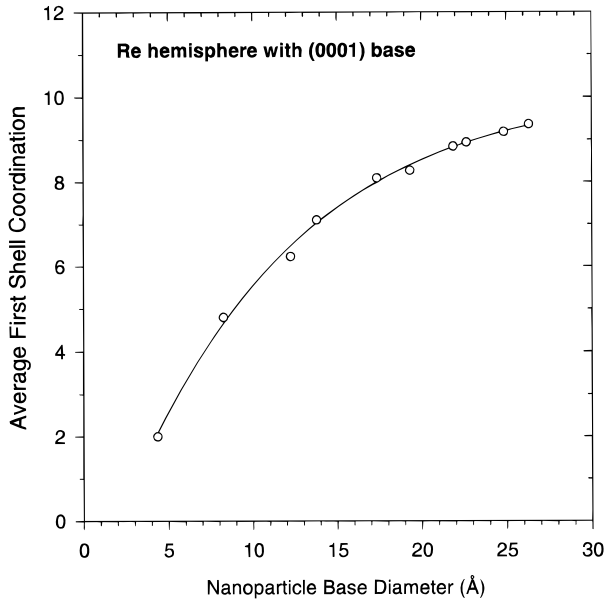

Figure 9. Average first-shell coordination numbers for a hcp Re hemisphere of specific diameter. The hemisphere is assumed to be oriented with the [0001] crystal lattice vector normal to the substrate surface.

that there are significant differences in the morphologies of the bimetallic nanoparticles obtained from each precursor. In each catalyst, Ir has consistently twice as many metal neighbors as does Re. For example, the total metal coordination numbers for Re and Ir in the activated [Re_7Ir-N] catalyst were 5.1 and 10.8, respectively. This is inconsistent with the phase separation of the two metals into large, predominantly Ir clusters and small, predominantly Re clusters, since in a cubic, close-packed sphere roughly 300 Ir atoms would be needed to give an average first shell coordination of 10.[25] Thus, the contrasting Re and Ir coordination environments in [Re_7Ir-N] must result from segregation of the Ir atoms to the core of nanoparticles with a relatively well-defined average diameter. It is possible to estimate this average particle size from a qualitative analysis of the higher shell scattering seen for the Ir and Re centers.

First shell coordination numbers can be directly related to average diameter in a model nanoparticle because of the large fraction of atoms that lie at its surface.[25−29] Figure 9 correlates the average first-shell coordination numbers for all metal atoms in a hcp hemisphere of Re atoms constructed in a manner following an analytical model similar to that of Van Zon et al.[26] An hcp crystal structure (i.e., that of bulk Re) was chosen as a model; as suggested by the data shown in Figure 2, distinguishing between fcc and hcp crystal structures is not possible for clusters of this size using EXAFS alone. The compositionally weighted average of the Re and Ir first-shell metal coordination for [Re_7Ir-N] gives an average metal coordination of 5.8. Based on the hcp hemisphere model, this is consistent with the formation of a "close-packed" nanoparticle with a diameter of at least 11 Å.

The theoretical EXAFS for the hcp hemisphere model nanoparticle is easily obtained by using the FEFF program with

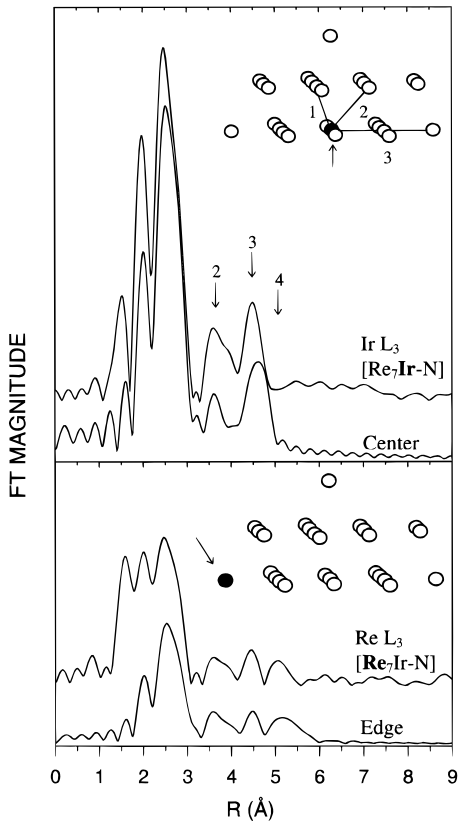

Figure 10. Calculated EXAFS for a metal (Re or Ir) atom located in the center and on the edge of a 26-atom close-packed hemisphere of Re atoms compared to measured EXAFS from the Ir and Re L_3-edges for the [Re_7Ir-N] catalyst.

the scattering functions of Re metal.[30] Figure 10 shows the calculated EXAFS data for an atom at the center (upper panel) and at the edge (lower panel) of such a particle. The central Ir atom, with 9 nearest neighbors, has a large magnitude for the first three shells, but zero magnitude for distances above 4.8 Å (R_3); such scattering in the model is strictly limited by the boundary of the particle. In contrast, the edge atom, with 3 nearest neighbors, shows significantly smaller first- through third-shell contributions, but significant scattering due to a shell at about 5.3 Å (R_4) is clearly evident.

As can be seen from this simulation, there is a very close resemblance between the model central-atom EXAFS and the measured Ir data for the fully activated [Re_7Ir-N] catalyst. Thus, it is notable that the local structure of the Ir atoms in the catalysts, up to the third shell, closely resembles that modeled on the basis of a bulk, close packed metal structure of finite size. It is also significant to note that in the Ir data there is no significant contribution to the EXAFS for shells past the third due to the finite size of the nanoparticle (this conclusion is strengthened by the excellent signal to noise ratio of the data), while conversely, the Re shows a marked fourth-shell contribution in the EXAFS. This is consistent with a large fraction of these latter atoms occupying sites at the edge of the nanoparticle. Though this model appears stoichiometically incorrect, it provides strong inferential evidence that the Ir atom must preferentially occupy core positions within the bimetallic nanoparticles. The key feature of the model, viz. the structure of the cluster, is that Re atoms show a significantly lower average metal coordination than Ir because they preferentially occupy surface sites of the nanoparticle while Ir occupies interior core positions.

(25) Benfield, R. E. *J. Chem. Soc., Faraday Trans.* **1992**, *88*, 1107.
(26) Van Zon, J. B. A. D.; Koningsberger, D. C.; van't Blik, H. F. J.; Sayers, D. E. *J. Chem. Phys.* **1985**, *82*, 5742.
(27) Sinfelt, J. H.; Via, G. H.; Lytle, F. W. *Catal. Rev. Sci. Eng.* **1984**, *26*, 81.
(28) Clausen, B. S.; Grabek, L.; Topsøe, H.; Hansen, L. B.; Stoltze, P.; Norskov, J. K.; Nielsen, O. H. *J. Catal.* **1993**, *141*, 368.
(29) Gallezot, P.; Bienenstock, A. I.; Boudart, M. *Nouv. J. Chim.* **1978**, *2*, 263.
(30) Rehr, J. J.; Albers, R. C. *Phys. Rev.* **1990**, *B41*, 8139.

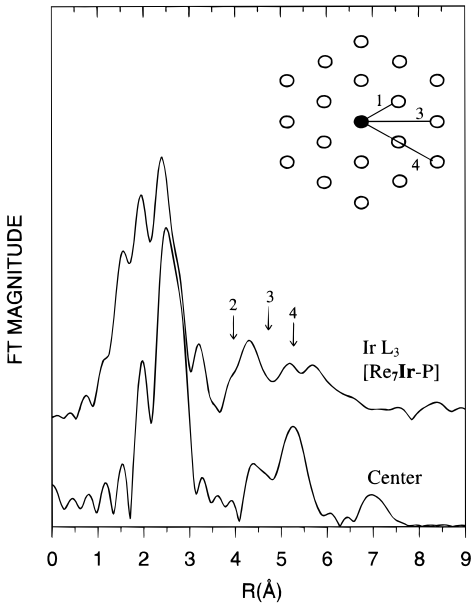

Figure 11. Calculated EXAFS for a metal (Re or Ir) atom located in the center of a 2-dimensional hexagonal arrangement of Re atoms compared to measured EXAFS of the Ir L_3-edge data for the [Re_7Ir−P] catalyst.

We conclude that the typical nanoparticle in the [Re_7Ir−N]-derived catalyst is at least 1 nm in diameter with a close-packed structure similar to that of Re metal. For a particle of this size, with the known composition of the starting carbonyl cluster, this suggests the average core contains 3−4 Ir atoms surrounded by as many as 28 Re atoms. We should note that there is always the possibility that larger particles exist, with disordered higher shells which do not contribute significantly to the EXAFS signal.

For the [Re_5IrRe_2−N] catalyst, the trends follow similarly. The bond distances around Ir are identical to the bond distances observed in [Re_7Ir−N] (Figure 3 and 4), the first shell coordination is reduced, however, by 20% and the third shell by 30%. The Re data also show a 30% reduction in the first shell coordination and very little higher shell structure. This suggests that the morphology around the Ir atoms is similar to that of [Re_7Ir−N], i.e., close-packed metal atoms with a core of Ir; however, the decreased amplitude of the metal shells implies a collection of fewer atoms and thus a smaller size of the average particle.

The catalysts derived from the PPN counterion ([Re_7Ir−P] and [Re_5IrRe_2−P]) show dramatically different shell structures around both the Re and Ir. The significantly reduced first shell coordination reflects a smaller average particle size forming upon reduction, a trend which is also evidenced in the Ir higher shell data. Interestingly, the Ir higher shell structure is not consistent with EXAFS from a three-dimensional close-packed structure. Specifically, scattering amplitude for the second coordination shell (R_2 = 3.89 Å) is weak (or even absent).

A simple model provides insight into these structural issues. Figure 11 compares the experimental Ir EXAFS with that calculated for a two-dimensional hexagonal arrangement of Re atoms. It is clear that significant scattering amplitude at an R_2 distance can only be obtained from a three-dimensional structure. We therefore suggest that the nanoparticles derived from the PPN salts must be both smaller (as judged by the absolute amplitude at R_1) and essentially two-dimensional.

One problem with a simple "raft-like" model for the PPN-derived catalysts is that the contribution to the EXAFS from bonding to low-Z elements does not vary significantly among the four catalysts. A short Re−O distance (2.1 Å) present in each catalyst is similar to the metal−oxygen distance formed in metal complexes with a μ_3-O[31] linkage but longer than the Re═O double bond distance (1.74 Å) found, for example, in the perrhenate ion, $[ReO_4]^-$.[32] The longer Re−O and Ir−O bond distance (2.5 Å) has been assigned previously by Koningsberger and Gates to the interaction of low oxidation-state metal species with the support.[33] We note, however, that there are no model molecular compounds of which we are aware that show either Re−O or Ir−O bond distances of this magnitude.

2. Evolution of Bimetallic Particle Nanostructure. The study presented herein suggests the activation of the supported clusters, $[Z]_2[Re_7IrC(CO)_{23}]$, proceeds via fragmentation of the cluster framework and subsequent growth of the close-packed bimetallic nanoparticle. However, differences in the fragmentation and nucleation processes are observed for the two isomers which in turn depend on the specific cluster framework as well as the associated counterions.

The important features in the IR spectra of the supported samples during activation are the disappearance of the CO stretching band of the parent cluster (2013 cm^{-1}), the appearance of an intermediate species (1985 cm^{-1}) which is removed by continued activation, and the appearance of a second species (2023 and 1914 cm^{-1}) which is the only species observable by IR spectroscopy for each sample at the high-temperature limit (573 K) of the IR study.

The fragment with CO bands at 2023 and 1914 cm^{-1} is assigned to a $M(CO)_3$ surface species by analogy with previous studies of $H_3Re_3(CO)_{12}$ supported on alumina which is reported to quantitatively produce a surface species nominally written as $Re(CO)_3\{O-Al\}\{HO-Al\}_2$; this latter moiety has two closely matching CO bands with maxima at 2027 and 1914 cm^{-1}.[34] The formation of $Re(CO)_3\{O-Al\}\{HO-Al\}_2$ has also been postulated for the species produced from the deposition of $\{Re(CO)_3(\mu_3\text{-}OH)_4\}_4$ onto alumina (2026 and 1921 cm^{-1}).[17] The intermediate species with the band at 1985 cm^{-1} is assigned as an octahedral metal carbonyl cluster based upon the similarity of the CO peak position with likely molecular analogs, such as $[Re_6C(CO)_{19}]^{2-}$ or $[H_2Re_6C(CO)_{18}]^{2-}$ (ca. 1985 cm^{-1} in acetone).[35]

The assignments made in the IR spectra indicate the activation of these metal clusters initially proceeds through a decapping process. The decapping process is one in which one or both of the exposed, face bridging $M(CO)_3$ caps are broken off of the parent cluster producing a surface bound $M(CO)_3$ group and leaving behind the more stable octahedral metal−carbide core. Additional support for this decapping process comes from recent transmission electron microscopy studies which have demonstrated the stability of supported $H_2Re_6C(CO)_{19}$ but showed that Re clusters with face capping groups ($[PPN]_3[Re_7C(CO)_{21}]$ and $[PPN]_3[Re_8C\ (CO)_{24}]$) undergo facile fragmentation.[36]

The TPDE profiles show two important features, both of which relate to the desorption of CO. The first feature is the

(31) (a) Xiao, J.; Hao, L.; Puddephatt, R. J.; Manojlovic-Muir, L.; Muir, K. W. *J. Am. Chem. Soc.* **1995**, *117*, 6316. (b) Ingham, S. L.; Lewis, J.; Raithby, P. R. *J. Chem. Soc., Chem. Commun.* **1993**, 166. (c) Cotton, F. A.; Lahuerta, P.; Sanau, M.; Schwotzer, W. *J. Am. Chem. Soc.* **1985**, *107*, 8284. (d) Goudsmit, R. J.; Johnson, B. F. G.; Lewis, J.; Raithby, P. R.; Whitmire, K. H. *J. Chem. Soc., Chem. Commun.* **1983**, 246.

(32) (a) Brown, R. J. C.; Segel, S. L.; Dolling, G. *Acta Crystallogr.* **1980**, *B36*, 2195. (b) Herrmann, W. A.; Roesky, P. W.; Kühn, F. E.; Elison, M.; Artus, G.; Scherer, W.; Romão, C. C.; Lopes, A.; Basset, J-M. *Inorg. Chem.* **1995**, *34*, 4701.

(33) Koningsberger, D. C.; Gates, B. C. *Catal. Lett.* **1992**, *14*, 271.

(34) Kirlin, P. S.; DeThomas, F. A.; Bailey, J. W.; Gold, H. S.; Dybowski, C.; Gates, B. C. *J. Phys. Chem.* **1986**, *90*, 4882.

(35) Hsu, G.; Wilson, S. R.; Shapley, J. R. *Inorg. Chem.* **1991**, *30*, 3881.

(36) Singal, A.; Gibson, J. M.; Treacy, M. M. J.; Lane, P. D.; Shapley, J. R. *J. Phys. Chem* **1996**, *100*, 6385.

presence of a low-temperature (575 K) CO desorption feature for each sample which coincides with the disappearance of the intermediate species seen in the infrared spectra (see above). The second feature is the high-temperature (750 K) desorption of CO which is present only in the PPN-containing samples. The disparity of the CO desorption in the high-temperature region between the PPN and TEA based samples indicates a fundamental difference exists in the final activation step between these two systems.

Insight into what this fundamental difference might be is obtained by examination of the TPDE profile of $\{Re(CO)_3(\mu_3\text{-}OH)\}_4$ supported on alumina (Figure 5).[37] As mentioned previously, supporting $\{Re(CO)_3(\mu_3\text{-}OH)\}_4$ on alumina is believed to quantitatively produce a mononuclear rhenium tricarbonyl species, nominally written as $Re(CO)_3\{O-Al\}\text{-}\{HO-Al\}_2$. This is also the only species observed in the high-temperature limit of the infrared study (573 K) for each catalyst sample. The TPDE profile for $\{Re(CO)_3(\mu_3\text{-}OH)\}_4$ supported on alumina is very similar to that of the PPN-based catalysts in the high-temperature region and includes the CO desorption which is absent in the TEA-based catalysts. By using supported $\{Re(CO)_3(\mu_3\text{-}OH)\}_4$ as a model for $M(CO)_3$ surface species, it is seen that the $M(CO)_3$ surface species present at 573 K in the IR spectrum of each sample stays as a $M(CO)_3$ surface species in the PPN-based catalysts but undergoes a process in which it is altered in the TEA systems. This process could be an agglomeration process which is inhibited in $[Re_7Ir-P]$ and $[Re_5IrRe_2-P]$ by the interaction of the highly dispersed metal particles with a residual phosphorus species (e.g., phosphate) from the PPN counterion.

The Re EXAFS and XANES data collected during activation of the TEA-based precursors also indicate the fragmentation of the precursor metal framework. Heating these precursors to 573 K in H_2 resulted in the replacement of the Re−metal bonds found in the cluster (average Re−M distance of ca. 2.9 Å) with Re−low-*Z* interactions (Figure 8) which result from bonding to the support and to remaining CO ligands. Consistent with the TPDE data, the CO interactions disappear upon heating to 623 K in H_2. In addition, the XANES data clearly indicate an increase in the number of unoccupied d-states for the Re atoms in this same temperature range. This change in the Re electronic structure may reflect an increase in the average oxidation state of the Re due to a larger fraction of the Re centers being bonded with the more electron withdrawing support ligands or an increase in the dispersion, i.e., the formation of smaller metal ensembles.[24d,e]

The nucleation of close-packed metal nanoparticles during the activation of the TEA-based samples is observed via the Ir EXAFS. In the $[Re_5IrRe_2-N]$ samples, Ir-metal bonding is present as low as 573 K and the coordination number increases steadily as the activation process is carried on to higher temperatures (Table 4). On the other hand, the Ir EXAFS data from the $[Re_7Ir-N]$ sample indicate that no significant metal contribution is present after heating to 573 K. Further heating of the $[Re_7Ir-N]$ catalysts to 623 K in H_2 results in the formation of metal coordination around the Ir centers, however. The above noted differences between the 573 K Ir EXAFS data for these two clusters are reflections of the differences in the location of the Ir atoms in the clusters precursors. Specifically, the incorporation of the Ir in the octahedral core may allow the formation of close-packed metal structures at lower temperatures.

The dissimilarity between the Ir and Re metal coordination numbers measured during activation indicate that the larger ordered nanoparticles formed from the TEA-based precursors nucleate preferentially at the Ir centers during activation. The formation of the metallic nanoparticle therefore appears to be limited by the migration of the fragmented Re species to the Ir centers which in turn may catalyze the reduction of mobile Re species. The more reducible Ir sites may simply provide a reduction site for the highly oxophillic Re atoms. These results are consistent with the XANES data which indicate the reduction of the Re centers above 600 K.

In addition to differences in the reducibility of the Re and Ir centers, the formation of an Ir core structure may be driven also by a stronger heteronuclear bond. For example, field ion microscope (FIM) studies of single Re atoms on Ir metal surface indicate an enhanced strength of the heteronuclear Re−Ir bond.[38,39] These trends in metal−metal bond strengths also appear to be mirrored in the chemistries of clusters **1** and **2**, where it has been found that there is a spontaneous skeletal rearrangement of **1** to **2** in solution, in which Ir goes from being bonded to three Re atoms to six Re atoms as shown in Chart 1.[13] It is interesting to note that Re and Ir do not form any bulk intermetallic[40] phases, as might be expected from the strong metal interaction strengths noted above; rather, Re dissolves about 40 to 50 wt % Ir into a solid solution at room temperature.[41]

The formation of segregated core structures finds precedent in other bimetallic systems.[42] For example, EXAFS investigations of $Pt-Re/Al_2O_3$ catalysts suggest that the bimetallic phase is composed of small Pt clusters with Re enriched on the surface. In the $Pt-Re/Al_2O_3$ system mobile Re_xO_y species have been proposed to nucleate (via reductive adsorption processes) on previously reduced Pt atoms or clusters during activation in H_2.[43] Anomalous X-ray diffraction studies of silica supported Pt−Re clusters further revealed the presence of fcc Re crystallites. Since bulk Re metal is hcp, it was concluded that Re nucleates epitaxially on Pt cores.[42e]

3. Catalytic Properties of the Bimetallic Nanoparticles. The kinetics of ethane hydrogenolysis over metal catalysts have been studied in detail, since C_2H_6 has only one C−C bond to undergo cleavage. Sinfelt and co-workers conducted the most extensive studies examining all of the group VIII metals as well as Re under comparable conditions.[14] These studies have led to the following general conclusions about the mechanism of the reaction on the metal surface: (1) H_2 adsorbs and dissociates reversibly; (2) C_2H_6 adsorbs dissociatively, presumably to C_2H_5 and H; (3) the initial C_2H_5 species undergoes further dehydrogenation to form C_2H_x and more surface H; (4) the C−C bond in the C_2H_x breaks and CH_y, CH_z species are formed, and the CH_y, CH_z species pick up surface H and desorb as CH_4.

The rate differences over different metals can be analyzed in detail in terms of the energetics for each of these steps.[44] Of critical importance are the relative energies of the H−M and C−M bonds, since H_2 adsorption/dissociation competes for the

(37) Lane, P. D.; Shapley, J. R. *J. Mol. Catal.* **1994**, *86*, 121.

(38) Wang, S. C.; Ehrlich, G. J. *J. Chem. Phys.* **1991**, *94*, 4071.

(39) Tsong, T. T.; Chen, C. L. *Nature* **1992**, *355*, 328.

(40) Okamoto, H. In *Binary Alloy Phase Diagrams*, 2nd ed.; Massalski, T. B., Okamoto, H., Subramanian, P. R., Kacprazate, L., Eds.; ASM: Materials Park, 1990; Vol. 3, pp 2345−6.

(41) Hansen, M. *Constitution of Binary Alloys*; McGraw Hill: New York, 1958.

(42) (a) Davis, R. J.; Boudart, M. *J. Phys. Chem.* **1994**, *98*, 5471. (b) Via, G. H.; Drake, K. F., Jr.; Meitzner, G.; Lytle, F. W.; Sinfelt, J. H. *Catal. Lett.* **1990**, *5*, 234. (c) Sinfelt, J. H.; Via, G. H.; Lytle, F. W.; Gregor, R. B. *J. Chem. Phys.* **1981**, *75*, 5527. (d) Sinfelt, J. H.; Via, G. H.; Lytle, J. *Chem. Phys.* **1980**, *75*, 4832. (e) Liang, K. S.; Chien, F. Z.; Hughes, G. J.; Meitzner, G. D.; Sinfelt, J. H. *J. Phys. Chem.* **1991**, *95*, 9974.

(43) Augustine, S. M.; Sachtler, M. H. W. *J. Catal.* **1989**, *116*, 184.

(44) Dumesic, J. A.; Rudd, D. F.; Aparicio, L. M.; Rekoske, J. E.; Treviño, A. A. *The Microkinetics of Heterogeneous Catalysis*; American Chemical Society: Washington, DC, 1993.

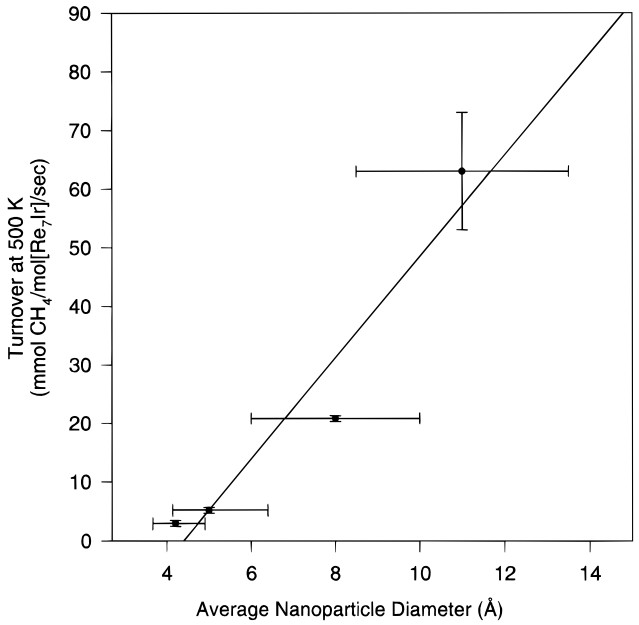

Figure 12. Correlation between average nanoparticle diameter versus the ethane hydrogenolysis TOF (see Table 1). Cluster size error bars were estimated from the relative error in the first-shell coordination numbers.

same metal sites as C_2H_6 adsorption/dehydrogenation. Since a number of metal centers must be involved in conducting both the H_2 and C_2H_6 activation, it is this requirement that gives ethane (alkane) hydrogenolysis its surface structure-sensitive or "demanding" character. In particular, there may be a critical ensemble size of metal atoms necessary for the overall C−C bond cleavage reaction.

Previous catalytic studies of alkane hydrogenolysis generally indicate a rate dependence on particle size. For example, the TOF of ethane hydrogenolysis increased monotonically with the diameter of Pt and Ir clusters supported on Al_2O_3.[45] More definitively, the hydrogenolysis of n-butane over a Ni/SiO_2 catalyst was shown to have a maximum activity for particles between 15 and 20 Å in diameter; for particles with diameter a of less than 10 Å there was no observed activity.[46,47] It has been concluded that a minimum of 20 Ni atoms were required for the hydrogenolysis of *n*-butane[46,48] and 12 Ni atoms were required for the hydrogenolysis of ethane.[48]

The data presented above reveal a rate sensitivity which is related to nanoparticle size for the four catalyst materials examined here. Figure 12 shows the TOF for the catalysts at 500 K for ethane hydrogenolysis plotted as a function of average nanoparticle diameter. The latter parameter was inferred from Figure 9. Thus, Figure 12 suggests that a significant portion of the strong rate dependence on precursor is related to the average nanoparticle size. It is not clear from the data whether there is a critical ensemble size of the nanoparticles necessary for the reaction to occur. The highly dispersed metal clusters derived from the PPN precursors may contain a small fraction of active metal ensembles, whereas the catalysts derived from the TEA precursors clearly contain a significant fraction of appropriate ensembles. Nevertheless, the EXAFS results which show large differences in the average cluster size are clearly supported by the differences seen in the catalytic activity.

Conclusions

Four different catalysts were derived from bimetallic clusters **1** and **2** with TEA and PPN as counterions. Using EXAFS, large variations were observed in the metal−metal coordination environments in the catalysts. The largest nanoparticles, derived from the TEA precursors, contain an Ir core surrounded by a three-dimensional cluster of up to 28 metal atoms. The two catalysts derived from the PPN precursors show smaller nanoparticles containing only a few metal atoms.

The rate of ethane hydrogenolysis increased approximately linearly with the average metal cluster size in the four catalysts. This result is consistent with previous studies, which have indicated that ethane hydrogenolysis requires adjacent active metal atoms to effect C−C bond scission.

The evolution of the bimetallic nanostructure for the TEA-based catalysts was probed by IR, XANES, TPR, and EXAFS. The results obtained using these techniques clearly demonstrate the fragmentation of the carbonyl cluster precursors and subsequent growth of a close-packed metal structure. The differences in the resulting catalyst structure suggest possible differences in the mechanisms of reduction in the two isomers. Specifically, the incorporation of the Ir in the octahedral carbide framework may affect the fragmentation of the clusters during activation and hence the rate of nanoparticle formation during the activation process.

Acknowledgment. This research was supported by grants from the U.S. Department of Energy, No. DEFG02-96ER45339, and the National Science Foundation, No. NSFDMR89−20538. The authors appreciate the *in situ* Lytle cell made available by EXXON. Further thanks go to Dr. Matthew Marcus for help collecting data on Re metal and to Dr. George Meitzner for his stimulating discussions. M.S.N. acknowledges a fellowship from the Department of Chemistry.

Supporting Information Available: Normalized, k^2-weighted Re and Ir EXAFS data with the associated Fourier-filtered first shell data, fits, and residuals (9 pages). See any current masthead page for ordering and Internet access instructions.

JA962174F

(45) Che, M.; Bennett, C. O. *Adv. Catal.* **1989**, *36*, 55.
(46) Romdhane, Y. H.; Bellamy, B.; de Gouveia, V.; Masson, A.; Che, M. *Appl. Surf. Sci.* **1988**, *31*, 383.
(47) Ryczkowski, J.; Gregorczyk, W.; Nuzimek, D. *Appl. Catal. A* **1995**, *126*, 341.
(48) Dalmon, J. A.; Martin, G. A. *J. Catal.* **1980**, *66*, 214.